J. Fluid Mech. (1974), *vol.* 64, *part* 2, *pp.* 319–345
Printed in Great Britain

Nonlinear cellular motions in Poiseuille channel flow

By J.-P. ZAHN,

Department of Mathematics, New York University and Astronomy Department, Columbia University, New York 10027†

JURI TOOMRE,

Department of Mathematics, New York University and Goddard Institute for Space Studies, New York 10025‡

E. A. SPIEGEL

Astronomy Department, Columbia University, New York 10027

AND D. O. GOUGH

Goddard Institute for Space Studies, New York 10025§

(Received 18 April 1973)

We expand the equations describing plane Poiseuille flow in Fourier series in the co-ordinates in the plane parallel to the bounding walls. There results an infinite system of equations for the amplitudes, which are functions of time and of the cross-stream co-ordinate. This system is drastically truncated and the resulting set of equations is solved accurately by a finite difference method. Three truncations are considered: (I) a single mode with dependence only on the downstream co-ordinate and time, (II) the mode of (I) plus its first harmonic, (III) a single three-dimensional mode. For all three cases, for a variety of initial conditions, the solutions evolve to a steady state as seen in a particular moving frame of reference. No runaways are encountered.

For Reynolds numbers below a critical value (2707 in case II), any initial disturbance to the parabolic profile dies away. For Reynolds numbers R and disturbance wavenumbers α for which linear theory predicts instability, an initial disturbance of any amplitude gives a particular, steady, finite amplitude solution. For R greater than the critical value mentioned above, but outside the linear instability region, 'subcritical instability' occurs for wavenumbers in a given band. That is, if the energy E of the initial disturbance to the parabolic profile exceeds a certain threshold, a steady finite amplitude solution is achieved as in the linearly unstable case. There is also a second finite amplitude steady solution with E equal to the threshold value. This is the subcritical solution discussed by several others and it is always unstable.

The loci of these steady finite amplitude solutions in R, α, E space are mapped out and their properties are outlined. The connexion between these solutions and previously discussed ones is briefly indicated and the question of their relevance to the development of observed instabilities is broached.

† Present address: Observatoire de Nice, 06300 Nice, France.

‡ Present address: Joint Institute for Laboratory Astrophysics, University of Colorado, Boulder, Colorado 80302.

§ Present address: Institute of Astronomy, University of Cambridge.

1. Introduction

A striking aspect of the breakdown of laminar flow in channels and pipes is that it leads directly to irregular or even turbulent motions. There is apparently no experimental evidence for the periodic nonlinear waves which would be analogues of the steady cellular motions seen at the onset of rotational (Taylor–Couette) or convective (Rayleigh–Bénard) instability, even though such analytic solutions do seem to exist for channel flow. The case of shear instability of channel flow is therefore a good example for making comparisons between these different kinds of transition to turbulence, especially since the linear theory is well understood (Lin 1955; Thomas 1953). There is also a considerable body of work (Stuart 1971) discussing nonlinear solutions to the equations of channel flow in which the velocity is decomposed into a mean part plus a nonlinear disturbance. The case where the disturbance flow has small amplitude has been treated extensively and it has been known for some time (Meksyn & Stuart 1951) that such solutions exist at Reynolds numbers below that at which linear theory first predicts instability of the Poiseuille profile. In these solutions, the disturbance flows are periodic (in time) in laboratory co-ordinates, but there exist Galilean frames in which they are steady.

In a plot of the square A^2 of the amplitude of the disturbance flow versus Reynolds number R every point on the R axis is a solution. The finite amplitude solutions bifurcate from the R axis in a direction of decreasing R and increasing A^2. The work of Meksyn & Stuart (1951) and of Grohne (1969) suggest that the finite amplitude branch of solutions goes down to some lower value of R and then turns parallel to the A^2 axis. These solutions are said to be subcritical (i.e. they occur at an R below the critical R of linear theory) and are manifestations of what is known as finite amplitude instability, though we prefer to call it metastability. Such behaviour is familiar in convection and Veronis (1966, 1968) has given a number of examples. It seems reasonable to speculate that, as in these examples of convection, the finite amplitude solution branch turns back towards higher R and A^2, so that in the region of metastability there are two 'steady' solutions. The analogy with the convective case goes even further with the demonstration by Chen & Joseph (1973) that the small amplitude nonlinear shear solutions are unstable just as in the convective cases studied by Busse (1967). However in the convective problem some of the larger amplitude solutions do seem to be stable and they (or something very like them) are seen in experiments. If the larger amplitude solutions exist equally in the case of channel flow it would be quite interesting to know why they are not seen. This question has motivated the present attempt to calculate such solutions and to derive some information about their stability. The techniques we use are related to those of previous work and before describing these we should report briefly on this background. Details are not needed since Stuart (1971) has given an extensive review of this work, while Monin & Yaglom (1971) provide a further excellent discussion of metastability in both channel flows and convection.

The principal approach to finite amplitude solutions is that of Stuart (1960) and Watson (1960). The disturbance flow is developed in Fourier series in the

downstream co-ordinate x and the series are truncated, typically, after two terms (fundamental and first harmonic). The equations resulting from these expansions are then developed in amplitude, and if the first nonlinear corrections are retained, the amplitude is given by

$$\partial A^2/\partial t = k_1 A^2 + k_2 A^4, \tag{1.1}$$

where k_1 and k_2 are constants. This equation was postulated by Landau (1944) to describe his physical picture of the transition to turbulence. Stuart's derivation provides explicit expressions for k_1 and k_2, which have been evaluated by Pekeris & Shkoller (1967), while an alternative, but related, development of the theory has been provided by Reynolds & Potter (1967). The values of k_2 turn out to be such that only in some parts of the linear instability region (where k_1 is of course positive) does (1.1) predict a stable nonlinear disturbance flow. Moreover, for all Reynolds numbers below the critical value for linear instability ($k_1 < 0$), Stuart's formula gives positive k_2. This predicts that disturbances with amplitude above a certain threshold will grow, seemingly without bound.

Other attempts to map out the nonlinear solutions of channel flow have taken Fourier or eigenfunction expansions as their starting points. Pekeris & Shkoller (1969*a*, 1971) used a three-mode Fourier representation in the downstream co-ordinate and, following a suggestion by Eckhaus (1965, p. 98), introduced a truncated Orr–Sommerfeld eigenfunction representation in the cross-stream co-ordinate. For disturbances of sufficiently large initial amplitude, their solutions grew without bound, not only in the Meksyn–Stuart region of metastability, but even at Reynolds numbers below which the parabolic profile showed no metastability according to Grohne or Meksyn & Stuart. This seems surprising, even in view of the prediction from (1.1), since the work of Pekeris & Shkoller does not *explicitly* have a small amplitude limitation. To us the conventional idea that in reality nonlinear effects intervene to place a limitation on the amplitudes of the disturbance flow remains attractive. To check this, one should ideally attempt to solve the Navier–Stokes equations, but here we shall undertake a far less ambitious approach to the problem. We shall represent the disturbance flow by drastically limited Fourier expansions in the downstream co-ordinate but shall solve the resulting equations (numerically) with high accuracy to obtain a good representation of the cross-stream structure of the solution. In particular, we shall show that indeed the nonlinear terms always limit the amplitude of the disturbance flow in this approximation. A similar effort has recently been made by George & Hellums (1972). They retained two downstream harmonics and treated the resulting equations by finite difference methods. Our approach differs from theirs chiefly in that we find steady solutions in certain Galilean frames whereas they followed the initial evolution in time (cf. also Dowell 1969) of solutions seen in the laboratory frame. By finding the steady solutions, we are able to map extensively the regions of metastability in the parameter space of solutions.

We recognize, of course, that convergence of the expansion we are using to a solution of the Navier–Stokes equations is not guaranteed. However, the

practical significance of this kind of approach does seem to be established and the rule of thumb that higher terms be small has been our guide. Thus, for $R < 10^4$, we find that the energy of the second downstream harmonic of the disturbance flow is always less than 1 % of the fundamental. But even at the lowest Reynolds numbers the mean velocity profile is markedly distorted, and we would not feel justified in making similar expansions in cross-stream harmonics. This structure has thus been treated with high precision by finite difference methods.

Having thus attempted to locate the place of the present effort in the context of the existing studies of channel flow, we turn in the next section to an explicit statement of the approximations. Then in § 3 we outline the numerical procedures used, and try to underline the key points that have seemed necessary for finding accurate solutions. In § 4 we give the results, mainly in graphical form, and finally, in § 5, we note some of the conclusions that we may draw and the questions they raise.

2. Approximations

We consider a flow driven through a channel by a fixed pressure gradient and choose the x co-ordinate in the direction of this gradient. The channel walls are at $z = +1$ and $z = -1$ and we use d, the half-width, as the unit of length. In this notation the laminar Poiseuille solution is $U_*(1-z^2)$ and we shall adopt U_* as the unit of velocity; the Reynolds number, which is then a measure of the imposed uniform pressure gradient $\partial_x p$, is given by

$$R = U_* d/\nu = -d^3 \partial_x p / 2\nu^2 \rho, \tag{2.1}$$

where ν is the kinematic viscosity.

The flows we study consist of a mean velocity U in the x direction plus a disturbance velocity $\mathbf{v}$ which may be described in terms of two scalar functions F and G; that is, the total velocity may be written as

$$\mathbf{v} = \mathbf{1}_x U(z,t) + \nabla \times \nabla \times [\mathbf{1}_z F(x,y,z,t)] + \nabla \times [\mathbf{1}_z G(x,y,z,t)], \tag{2.2}$$

where $\mathbf{1}_z$ is a unit vector in the z direction. For the scalar functions F and G we take the following decomposition:

$$F = \mathrm{Re} \sum_{k=1}^{\infty} a_k^{-2} f_k(x,y)\, \Omega_k(z,t), \quad G = \mathrm{Re} \sum_{k=1}^{\infty} a_k^{-2} \partial_y f_k(x,y)\, \Phi_k(z,t), \tag{2.3}$$

where $f_k(x,y)$ is the most general harmonic planform of total wavenumber a_k such that

$$(\partial_x^2 + \partial_y^2) f_k = -a_k^2 f_k. \tag{2.4}$$

In addition, we impose the orthonormality condition

$$\overline{f_i f_j^*} = 2\delta_{ij}. \tag{2.5}$$

(The overbar stands for a spatial average over x and y and the asterisk denotes a complex conjugate.) We note that the z components of the disturbance velocity and the vorticity are given by

$$\mathbf{1}_z . \mathbf{v} = \mathrm{Re} \sum_{k=1}^{\infty} f_k \Omega_k, \tag{2.6}$$

$$\mathbf{1}_z . \nabla \times \mathbf{v} = \mathrm{Re} \sum_{k=1}^{\infty} \partial_y f_k \Phi_k. \tag{2.7}$$

In cases where the disturbance is two-dimensional (depending only on x and z), the disturbance stream function is

$$\Psi = \partial_x F = \mathrm{Re} \sum_{k=1}^{\infty} a_k^{-2} \partial_x f_k \Omega_k. \tag{2.8}$$

Substitution of these expansions into the Navier–Stokes equations, followed by the usual projections, yields a set of partial differential equations in z and t for U and the Ω's and Φ's. We shall exhibit these equations only for the cases treated here, where the horizontal planforms are restricted to the simple forms

$$f_k = N_{\alpha\beta} \cos \beta y \, e^{-ik\alpha x}, \quad a_k^2 = k^2\alpha^2 + \beta^2, \tag{2.9}$$

where $N_{\alpha\beta}$ is the normalization constant appropriate to the horizontal spatial frequencies α and β. We also apply a Galilean transformation to a co-ordinate frame moving in the positive x direction with a speed c to be specified. The equation for U is then

$$\partial_t U + \partial_z \sum_{k=1}^{\infty} \frac{ik\alpha}{2a_k^2} (\Omega_k \partial_z \Omega_k^* - \Omega_k^* \partial_z \Omega_k) - \partial_z \sum_{k=1}^{\infty} \frac{\beta^2}{2a_k^2} (\Omega_k \Phi_k^* + \Omega_k^* \Phi_k) - R^{-1}(\partial_z^2 U + 2) = 0. \tag{2.10}$$

The equations for the Ω's and the Φ's are

$$\partial_t \mathscr{D}_k \Omega_k + ik\alpha[(\partial_z^2 U)\,\Omega_k - (U-c)\,\mathscr{D}_k \Omega_k] - R^{-1} \mathscr{D}_k^2 \Omega_k = \{S_k\}, \tag{2.11}$$

$$\partial_t \Phi_k - ik\alpha(U-c)\,\Phi_k - (\partial_z U)\,\Omega_k - R^{-1} \mathscr{D}_k \Phi_k = \{T_k\}, \tag{2.12}$$

where

$$\mathscr{D}_k = \partial_z^2 - a_k^2. \tag{2.13}$$

$\{S_k\}$ and $\{T_k\}$ represent the nonlinear terms which couple the different k components or modes; their general form is intricate and they will be given explicitly below for the cases considered here. When $\partial_t = 0$, and the coupling terms are neglected, (2.11) becomes the Orr–Sommerfeld equation. We emphasize that U is the mean flow as seen in the laboratory frame, and that hereafter the perturbation velocity is as seen in the frame moving at speed c.

We may now list the three main problems whose solutions are to be discussed.

(I) *One-mode problem.* Here the disturbance consists of a single (complex) roll with its axis aligned in the y direction. This is the simplest truncation which couples the disturbance and the mean velocity and for which the disturbance flow is two-dimensional. In this case

$$f_1 = 2^{\frac{1}{2}} e^{-i\alpha x}, \quad a_1 = \alpha, \tag{2.14}$$

the Φ_1 equation is ignored and $\{S_1\} = 0$. This case yields the mean-field equations, which have also been studied by Meksyn & Stuart (1951) and Grohne (1969).

(II) *Two-mode problem.* To the transverse roll of problem I we add its first overtone in x. Thus we have

$$f_k = 2^{\frac{1}{2}} e^{-ik\alpha x}, \quad a_k = k\alpha, \quad k = 1, 2, \tag{2.15}$$

and the equations for the Φ's are again not needed. The coupling terms take the following form:

$$\begin{aligned}\{S_k\} = &-\frac{1}{2^{\frac{1}{2}}} \sum_{l+m=k} \frac{k}{m} [\Omega_l \partial_z \mathscr{D}_m \Omega_m - (\mathscr{D}_l \Omega_l)\, \partial_z \Omega_m] \\ &+ \frac{1}{2^{\frac{1}{2}}} \sum_{l-m=k} \frac{k}{m} [\Omega_l \partial_z \mathscr{D}_m \Omega_m^* - (\mathscr{D}_l \Omega_l)\, \partial_z \Omega_m^*] \\ &- \frac{1}{2^{\frac{1}{2}}} \sum_{m-l=k} \frac{k}{m} [\Omega_l^* \partial_z \mathscr{D}_m \Omega_m - (\mathscr{D}_l \Omega_l^*)\, \partial_z \Omega_m].\end{aligned} \tag{2.16}$$

Since the triad coupling terms $\{S_k\}$ are now present, the problem is no longer of the mean-field type. This case uses the same truncation as Stuart (1960) and Watson (1960), retaining only two downstream Fourier modes. They showed that the resulting equations are valid at least for small amplitudes. Our goal is to study the solutions of these equations at larger amplitudes, though points of contact will be made at small amplitudes with the results of Reynolds & Potter (1967), Pekeris & Shkoller (1967, 1969*b*) and Chen & Joseph (1973).

(III) *A three-dimensional example.* In this case we have both x and y structure in the disturbance flow:

$$f_1 = 2 \cos \beta y\, e^{-i\alpha x}, \quad a_1 = (\alpha^2 + \beta^2)^{\frac{1}{2}}, \tag{2.17}$$

and the coupling terms vanish: $\{S_1\} = \{T_1\} = 0$. This case is again a mean-field problem with crossed rolls. The solutions of this three-dimensional analogue of case I will be compared with similar ones by Grohne (1969). We emphasize that this is the simplest one-mode three-dimensional example; other cases exist with self-interactions which may give stronger advective effects.

In § 4 we shall give detailed results for cases I and II and only indicate how case III differs from these. In presenting the results we shall split the Ω's and Φ's into their real and imaginary parts:

$$\Omega_k = W_k + i\tilde{W}_k, \quad \Phi_k = Z_k + i\tilde{Z}_k. \tag{2.18}$$

Further, we shall use the following functions which are related to the y component of vorticity in cases I and II:

$$Y_k = \mathscr{D}_k W_k, \quad \tilde{Y}_k = \mathscr{D}_k \tilde{W}_k. \tag{2.19}$$

The non-dimensional mass flux will be defined by

$$M = \frac{1}{2} \int_{-1}^{+1} U\, dz, \tag{2.20}$$

where $M = \frac{2}{3}$ for parabolic flow.

The energy of the mean flow will be measured by

$$E_U = \frac{15}{16} \int_{-1}^{+1} U^2\, dz, \tag{2.21}$$

where the coefficient is chosen so that $E_U = 1$ for parabolic flow. Similarly, the energy of the perturbation flow in the frame moving at speed c will be measured by

$$E = \frac{15}{16}\int_{-1}^{+1}(u^2+v^2+w^2)\,dz$$
$$= \sum_k (E_{Wk}+E_{Zk}), \tag{2.22}$$

where
$$E_{Wk} = \frac{15}{32}\int_{-1}^{+1}(a_k^{-2}|\partial_z\Omega_k|^2+|\Omega_k|^2)\,dz, \tag{2.23}$$

$$E_{Zk} = \frac{15}{32}\int_{-1}^{+1}\beta^2 a_k^{-2}|\Phi_k|^2\,dz, \tag{2.24}$$

and where (u, v, w) are the components of the disturbance flow in the frame moving at speed c.

The boundary conditions in all cases are that the Ω_k, Φ_k, $\partial_z\Omega_k$ and U all vanish on $z = \pm 1$. Various initial conditions are considered as explained in § 3.

(IV) *Transport of a passive scalar.* A small additional calculation that we have performed is that of the transport of a passive scalar T in case I. In this case, the z component of the perturbation velocity is simply

$$w = W_1\cos\alpha x + \tilde{W}_1\sin\alpha x, \tag{2.25}$$

and the scalar is expressed as

$$T = \bar{T}(z,t)+\theta_1(z,t)\cos\alpha x+\tilde{\theta}_1(z,t)\sin\alpha x. \tag{2.26}$$

The differential equations for these additional functions are

$$\partial_t\bar{T}+\partial_z(W_1\theta_1+\tilde{W}_1\tilde{\theta}_1) = P^{-1}\partial_z^2\bar{T}, \tag{2.27}$$

$$\partial_t\theta_1+W_1\partial_z\bar{T} = P^{-1}\partial_z^2\theta_1, \tag{2.28}$$

with a similar equation for $\tilde{\theta}_1$. The quantity

$$P = U_* d/\kappa = (\nu/\kappa)R \tag{2.29}$$

is the Péclet number, when κ is the thermal diffusivity. The boundary conditions are that $\bar{T} = 0$ at $z = 1$ and $\bar{T} = 1$ at $z = -1$, while θ_1 and $\tilde{\theta}_1$ both vanish at $z = \pm 1$. The quantity of principal interest is the transport of $\bar{T}$ across the channel resulting from the disturbance flow. This is measured by N (the Nusselt number if T is temperature):

$$N = -\partial_z\bar{T}+W_1\theta_1+\tilde{W}_1\tilde{\theta}_1, \tag{2.30}$$

where W_1 and $\tilde{W}_1$ are simply taken from the solution for case I for this calculation.

3. Numerical method

This section outlines the numerical procedure used in integrating any of the four systems of equations derived in § 2. All of these nonlinear partial differential equations, parabolic in classification, with time t and the cross-stream spatial co-ordinate z as the independent variables, are solved using finite difference representations.

An accurate spatial resolution can be achieved by finite difference methods provided that a stretched spatial mesh in z is used. The increasingly narrow boundary-layer structures encountered as R is increased can be resolved by defining a new independent variable $\xi(z)$, for which the M grid points (M is of order 300) are evenly spaced, so that the boundary-layer regions near the walls $z = \pm 1$ each begin to occupy about one-third of the ξ interval of $[-1, +1]$. All spatial derivatives are expressed by second-order-accuracy (local Δz definition) centred differences conveniently written in the ξ variables. The continuous and monotonic transformations between ξ and z are based upon smoothed cubic functions, as illustrated in figure 10. The extent of the cubic stretching is evident on realizing that, at $R = 10^4$ and $\alpha = 1{\cdot}00$, each boundary layer occupies of the order of 10 % of the z domain, while at $R = 10^8$ this value is reduced to 0·5 %.

Implicit time representations are used in which all differential spatial operators are evaluated at the same two time levels, ranging from a time-centred scheme which minimizes numerical diffusion to the very stable but diffusive fully implicit scheme. Such implicit time methods are required for these high resolution stretched spatial grids because the diffusive stability criterion $[\Delta t \leqslant 0{\cdot}5(\Delta z_{\min})^2]$ would otherwise imply prohibitively small time integration steps Δt. The finite difference forms of the boundary conditions for the time-dependent calculations were readily implemented, the Neumann conditions on W_k and $\tilde{W}_k$ being used to infer conditions on Y_k and $\tilde{Y}_k$.

The resulting nonlinear difference equations are solved at each time step by a Newton–Raphson iteration (cf. Henrici 1962, p. 366) leading to the repeated inversion of a large $(M \times M)$ block tridiagonal matrix. It should be remarked that the tridiagonal structure results from our preference for dealing with systems of equations involving second-order spatial differential operators, and thus each block in case I is 5×5, and in case II is 9×9. The iterative procedure has the advantage that it can also be employed in seeking steady solutions directly from the time-independent version of the equations.

As implied in § 2, the frame of reference may be chosen to move with the phase velocity inherent in these solutions. Such a Galilean transformation is found to be crucial in permitting the computation to proceed efficiently to viscous time scales of $O(R)$ by relaxing the $O(1)$ time step constraint otherwise dictated by wave propagation. A procedure was devised which could update the Galilean frame to reflect the possible time variation of the phase velocity c. The instantaneous phase ϕ of the complex function $\Omega_1 = W_1 + i\tilde{W}_1$ possesses the time derivative $\partial_t \phi = \partial_t \arctan(\tilde{W}_1/W_1)$, which is $\alpha \Delta c$, where Δc is the phase velocity with respect to the current Galilean frame. The increment Δc, determined from the present time derivatives of W_1 and $\tilde{W}_1$, is then applied to c to at least temporarily filter out the fast time variation.

As will be discussed in the next section, we found that a selection of initial-value problems for differing R and α showed complicated time evolutions that finally led to steady solutions in an appropriate frame moving with the phase velocity c. Wishing to exploit this property of the solutions, we also sought steady solutions by directly solving equations which were time-independent, but in which c had to be simultaneously determined. Sequences of such steady

solutions were constructed by suitably modifying the fields and the phase velocity of a steady solution at a neighbouring (R, α) point to provide the initial estimates for the Newton–Raphson iteration. Usually five or six iterations sufficed in this quadratically convergent scheme, requiring of the order of 3 s (for case I with $M = 300$) of IBM 360/95 machine time to obtain one solution. Most steady solution surveys were speeded up by computing only in the half-space $[0, +1]$, while assuming appropriate symmetry conditions for the solutions.

The imposition of boundary conditions for the time-independent equations deserves some comment. The *steady* problem is a real ordinary differential system of order $n = 12m + 2$, where m is the number of modes retained, and involving the phase velocity c, in effect an eigenvalue to be determined. The vanishing of the real and imaginary parts of Ω_k, Φ_k and $\partial_z \Omega_k$ at both boundaries imposes $12m$ boundary conditions. The remaining three boundary conditions are the vanishing of U on both boundaries, and an arbitrary condition on the phase of the fluctuating fields which serves to constrain the origin of time. However, it is convenient to remove c completely from the equations by using $U - c$ rather than U as the dependent variable, though c now enters in the boundary conditions. Since c is a constant, one can readily integrate the steady version of (2.10), and with symmetry considerations then obtain one boundary condition on the z derivative of $U - c$. The imposition of an arbitrary phase on the complex function Ω_1, for instance, supplies the remaining boundary condition. Finally, the value of $U - c$ on the boundary yields c.

4. Results of the calculations

In this section we present the results obtained from numerical solutions of (2.10)–(2.13) for the various cases discussed in § 2. We have carried out time-dependent calculations for a variety of initial conditions, and found that the solutions in all the cases studied either died away completely or became steady in some Galilean frame. Accordingly we have concentrated on the steady solutions, and most of the results reported in this section refer to steady solutions constructed directly from the time-independent equations. We further choose to emphasize cases I and II, in which the disturbance flows are periodic in x with period $2\pi/\alpha$ and are independent of y. In figure 1 we show the usual stability diagram in the R, α plane for these two cases. The shaded section is the familiar linear instability region. The two other curves demarcate the regions in which the one-mode (case I) and two-mode (case II) solutions can be sustained. Each of these regions consists of both the linear instability strip and a zone in which the flows are metastable, or finite amplitude unstable. The critical Reynolds numbers for metastability are about half the critical values given by linear instability theory; the various values are shown in table 1. The one-mode critical R and α are in good agreement with those of Grohne (1969). At the critical points for metastability, there is already some departure from the Poiseuille profile as indicated by U_0, the value of the mean velocity at mid-channel. (For the parabolic profile $U_0 = 1$.) The table also gives the mean and fluctuating kinetic energy densities E_U and E [cf. (2.21) and (2.22)] at the critical points. The r.m.s.

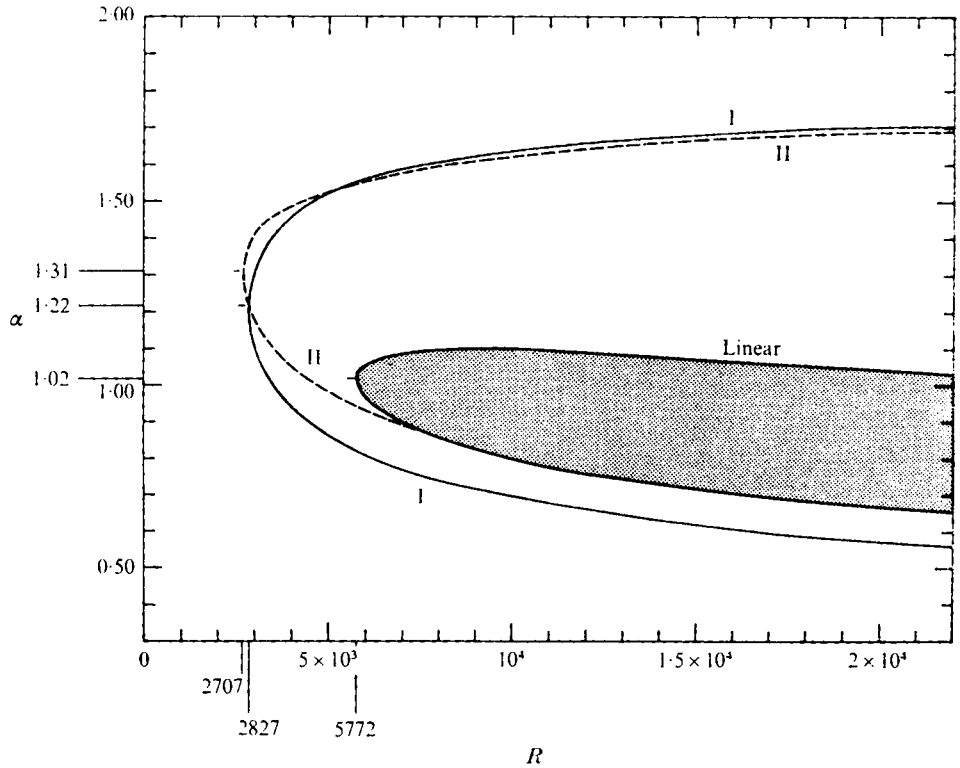

FIGURE 1. The regions of metastability from the one- and two-mode calculations are shown in the R, α plane. The shaded region is the instability loop of linear theory. Between this loop and the curves marked I and II the parabolic flow is metastable according to the calculations for cases I and II respectively (cf. §2). Anywhere in the interior of curves I and II, steady nonlinear cellular solutions are found in the corresponding approximation. The 'noses' of the various curves are indicated by tick marks and their coordinates are given at the edge of the figure; these are summarized in table 1.

Critical parameters	Linear	Case I (one mode)	Case II (two modes)	Grohne (one mode)
R	5772·22	2827·36	2706·65	*
$\hat{R}$	5772·22	2543·57	2471·17	2510
α	1·0206	1·2220	1·3126	1·218
U_0	1·0000	0·8996	0·9130	*
c/U_0	0·2640	0·3844	0·4011	0·393
E	0	$1·119 \times 10^{-2}$	$9·220 \times 10^{-3}$	*
E_U	1·0000	0·7841	0·8081	*

TABLE 1. The critical parameters associated with the 'nose' of the linear instability strip, contrasted with those of the steady finite amplitude solutions of cases I and II associated with the noses of their respective metastability regions. The maximum velocity U_0 at mid-channel and the phase velocity c, as all the velocity fields, are here normalized by U_*, the maximum velocity of the corresponding parabolic flow. The fluctuating and mean kinetic energies E and E_U are similarly scaled by the energy of that unperturbed flow. The usual laboratory Reynolds number $\hat{R}$ is based on the maximum value of the mean velocity, and thus $\hat{R} = U_0 R$. The linear parameters are those reported by Pekeris & Shkoller (1969*a*), as further refined by Orszag (1971). The asterisks indicate values unavailable in Grohne (1969).

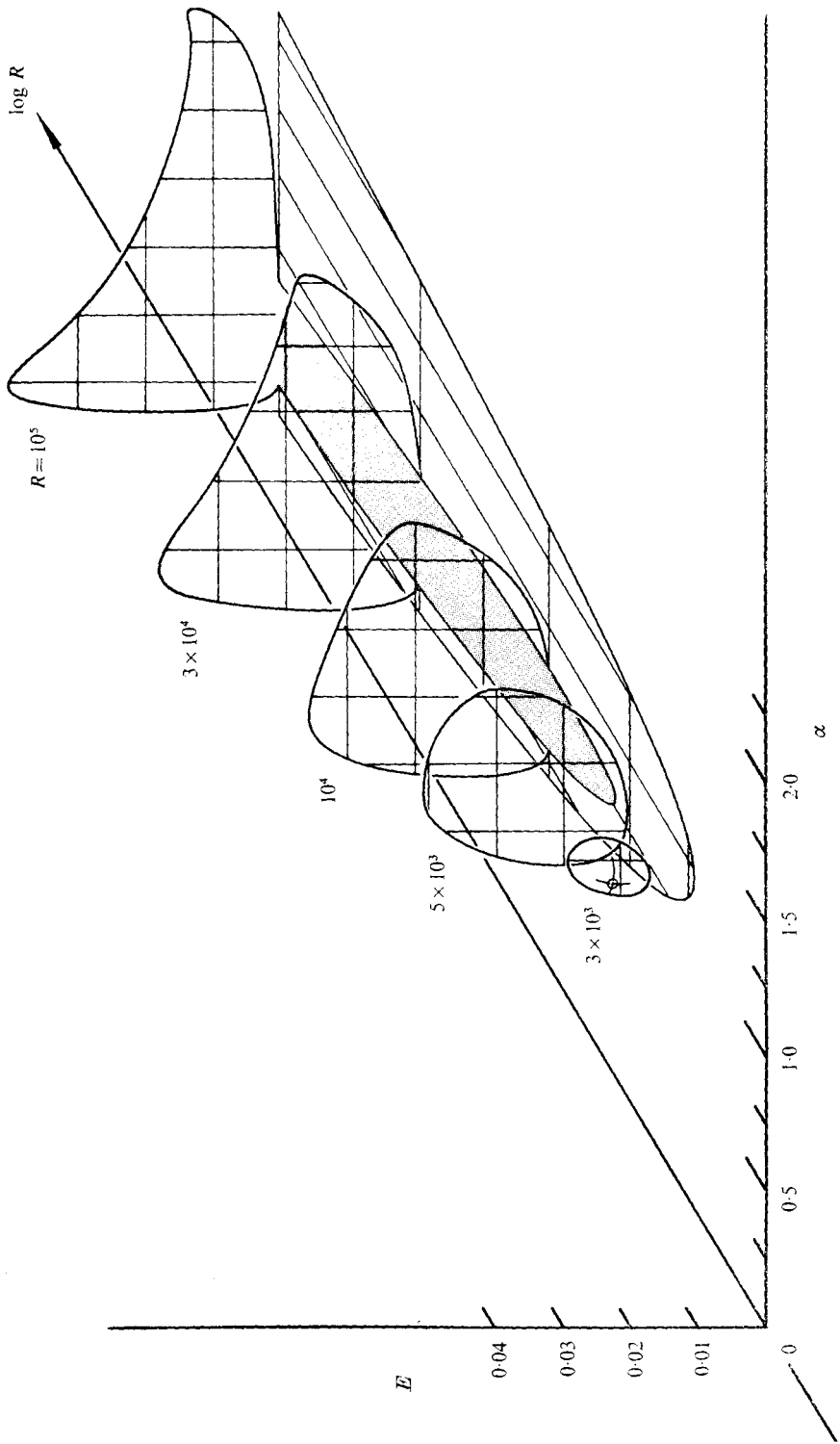

FIGURE 2. Illustrating the solution surface on which finite amplitude steady solutions are found in the one-mode approximation (case I). The vertical co-ordinate is the disturbance energy E [cf. (2.22)]. The linear instability loop and the region of metastability for case I shown in figure 1 are indicated in the $E = 0$ plane.

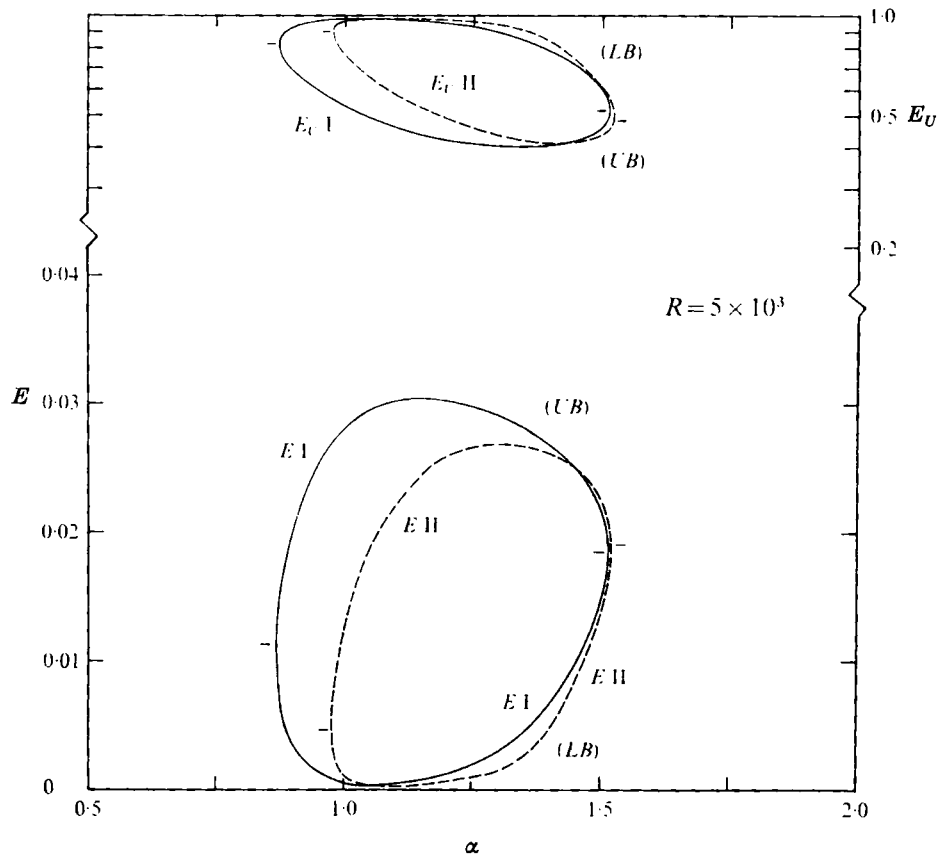

FIGURE 3. Energies *vs.* wavenumber α at $R = 5 \times 10^3$ for the steady finite amplitude solutions for cases I and II. The lower curves show the disturbance energy E while the upper curves show the mean energy E_U. Note that the solutions with larger disturbance energies are those with the smaller mean energies. At this R linear theory predicts stability. The ticks delineate the upper (UB) and lower (LB) solution branches. As in most of the figures, curves marked as I or II refer to the appropriate solution properties of cases I or II respectively.

total fluctuating velocity scaled by U_* is $(\frac{8}{15}E)^{\frac{1}{2}}$; its value is 0·0772 at the critical point for case I, which is comparable with the value 0·084 given in the early work of Meksyn & Stuart (1951) for the r.m.s. streamwise fluctuating velocity.

The value of E at the critical point for case II is essentially that of the first mode or fundamental; the contribution to the energy from the second mode is only about 0·14 %. In spite of the relatively small amplitude of the second mode, the critical curves for the one- and two-mode cases are somewhat different at the lowest α. The change is such that the lower part of the two-mode critical curve actually joins the corresponding branch of the linear neutral curve, while the one-mode metastability region entirely surrounds the linear instability domain.

Within the region of metastability computed in case I it was always possible to find two steady finite amplitude solutions. In the linear region only a single steady finite amplitude solution was realized. These results for case I are illustrated

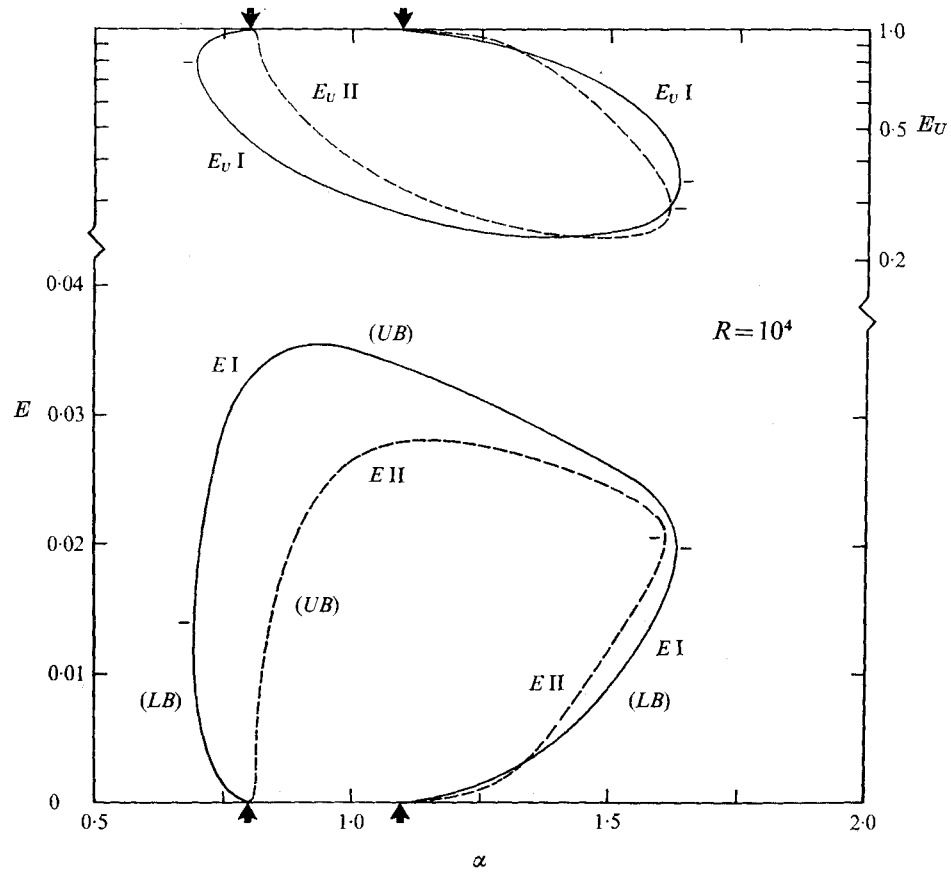

FIGURE 4. The same as figure 3, but for $R = 10^4$. The arrows show the limiting wavenumbers α between which linear theory predicts instability. The case I and II solutions are markedly different near their smaller α bifurcation point with the zero disturbance amplitude (parabolic profile) solution, here coincident with the arrows on the left. The case I *LB* solutions extend toward subcritical wavenumbers, while those of case II are *UB* solutions which go towards larger α and thus remain supercritical. In contrast, at the position indicated by the arrows on the right, cases I and II bifurcate as rather similar *LB* solutions towards subcritical α.

in figure 2, which shows the fluctuating energy E as a function of R and α. The shaded linear strip of figure 1 is indicated in the $E = 0$ plane; the extended range of R in this figure shows the broadening in α of the metastability region with increasing R.

For the purposes of comparing the one- and two-mode cases we present in figures 3, 4 and 5 three slices of the solution surface at fixed R, as well as analogous plots with the mean energy E_U in place of E. For comparison, the corresponding sections of the one- and two-mode energy surfaces are shown. The tick marks indicate the energies at the limits of the metastability regions. These marks divide the individual slices of the energy surfaces into two branches, the upper branches (*UB*) and lower branches (*LB*), which possess markedly dissimilar stability characteristics.

The difference between the stability characteristics of the *UB* and *LB* solutions appeared strikingly in the time-dependent solutions. For a variety of initial conditions these always evolved to *UB* solutions, while *LB* solutions could be found only by solving the steady equations. However, various stability tests were also applied. In addition to the conventional procedure of adding various small perturbations to all the fields, the stability of the steady solutions was studied as follows. A given steady solution was perturbed by multiplying the disturbance velocities by factors ranging from 0·9 to 1·1 while leaving the mean profile unchanged. This modified solution was taken as an initial condition for solving the time-dependent equations. All the *UB* solutions in cases I and II that were so perturbed returned to their original states. However, they did this by following extremely tortuous routes, oscillating, varying their phase velocities and developing internal boundary layers. As a result, adequate spatial and temporal resolution was needed to follow the evolution, and failure to provide this caused the solutions to grow without bound. Because of these complexities the stability studies were carried out only for $R \lesssim 10^5$. Perturbations of the *LB* solutions which represented an *increase* in amplitude by even as little as 2 % resulted in a similarly complex behaviour but with the end result that the solutions went to the upper branch. A *decrease* in the amplitude of an *LB* solution led to a temporal decay with the disturbance flow dying away completely.

Such calculations do not provide full stability information since the perturbations have the same planform as the original solution. However, they do indicate rather clearly that the *UB* solution is preferred in cases of non-uniqueness. Moreover, these studies give an indication of the perturbation amplitude necessary to drive the flow from the parabolic form to the states discussed here. If a perturbation on the parabolic flow has enough energy to raise it to the lower branch of the energy surface, it can proceed from there to become finally a finite amplitude steady disturbance flow on the upper branch of the surface.

These stability calculations of the *UB* and *LB* solutions are consistent with the analytic predictions by Chen & Joseph (1973) that a finite amplitude solution which bifurcates from the zero amplitude solution is unstable to small disturbances if it lies outside the linear loop (and thus subcritical), and stable if inside (supercritical). The calculations were performed before we became aware of their work. Chen & Joseph further conjecture that the flow would snap through such unstable solutions towards 'turbulent solutions' with a larger norm for their energy. The present calculations in fact explicitly show that if an *LB* solution is perturbed in a manner *increasing* the disturbance amplitude, this solution evolves toward a stable higher energy *UB* solution. Our results emphasize that a threshold energy (coincident with that of the *LB* solution) must be reached before a *UB* solution can be attained, though these results may be rather specialized owing to the simple one- and two-mode downstream structures studied.

One difference between figures 3 and 4 is that the former, at $R = 5 \times 10^3$, illustrates a subcritical R, in the sense of linear theory, while the latter, at $R = 10^4$, shows how the energy surface is related to the linear stability curve at supercritical R. The arrows in figure 4 delimit the linear instability band, and

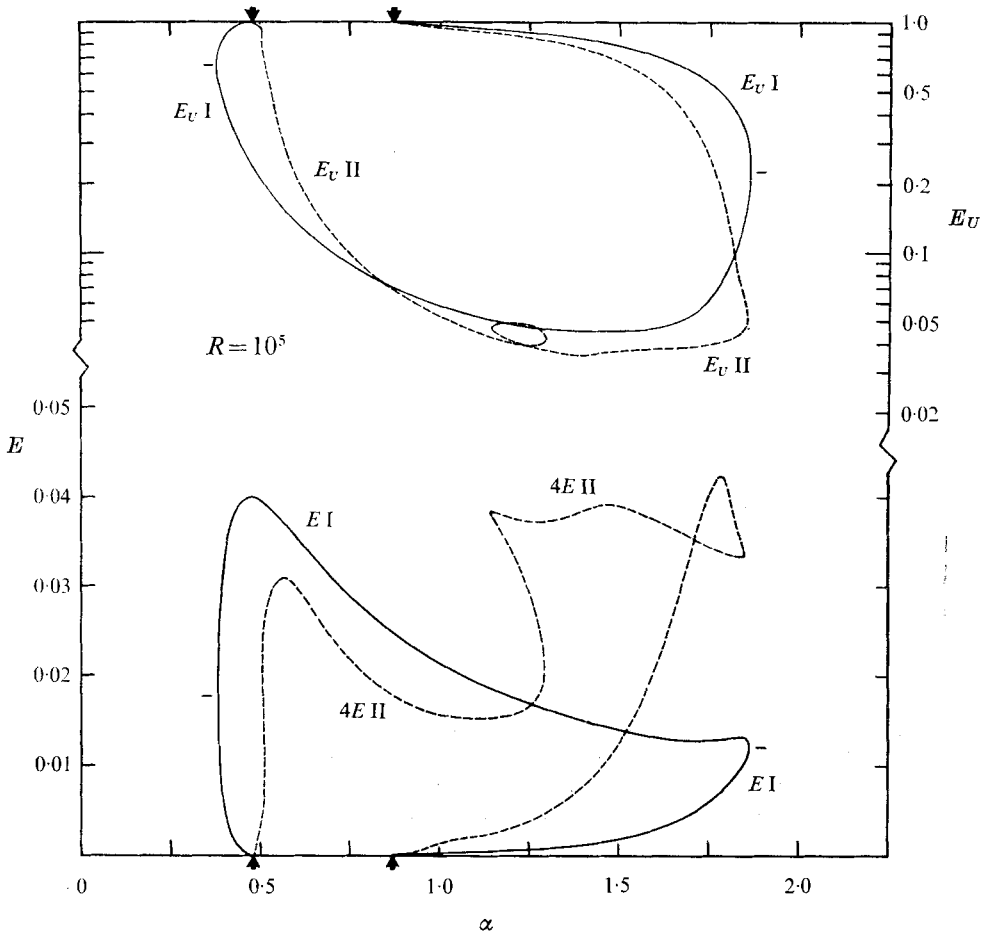

FIGURE 5. The same as figures 3 and 4, but at $R = 10^5$. Note that the plotted values show E for case II multiplied by a factor 4 and that cases I and II give disparate solutions for this R.

as expected, the energy surfaces join its edges at $E = 0$. Thus at $R = 10^4$ the band $0{\cdot}800 \leqslant \alpha \leqslant 1{\cdot}095$ is linearly unstable. The bands in which nonlinear solutions may be sustained are $0{\cdot}698 \leqslant \alpha \leqslant 1{\cdot}633$ for one mode and $0{\cdot}800 \leqslant \alpha \leqslant 1{\cdot}615$ for two modes. It is perhaps of interest to contrast the latter with the α band $0{\cdot}753 \leqslant \alpha \leqslant 0{\cdot}930$ in which Pekeris & Shkoller (1967) find that nonlinear terms are stabilizing on the basis of small amplitude two-mode calculations. Figure 4 also shows that the one-mode solutions possess a narrow metastability band for α below the linear neutral curve, whereas the two-mode solutions do not. The behaviour of the two-mode energy surface near the neutral curve is essentially as predicted by Pekeris & Shkoller (1969*b*) and Chen & Joseph (1973).

At the Reynolds numbers for figures 3 and 4, the harmonic second mode in case II continues to contribute only a small part of the disturbance energy. As R increases, the relative amplitude of the second mode grows so that at $R \simeq 10^5$ the second mode in case II has energy about one-third that of the fundamental,

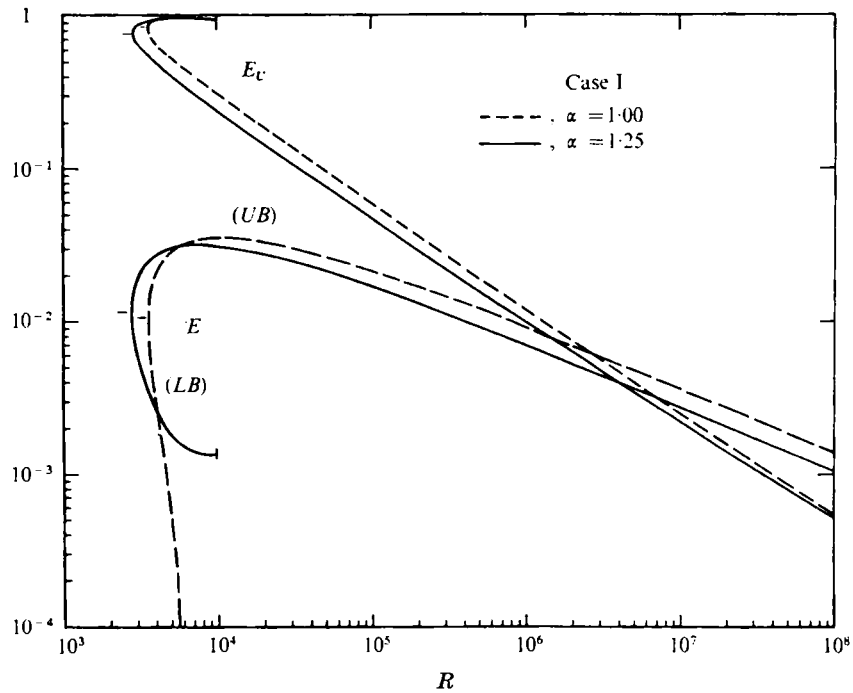

FIGURE 6. Showing the disturbance energy E and the mean energy E_U as functions of R for case I (one mode) at two fixed wavenumbers α. The line $\alpha = 1{\cdot}00$ in the R, α plane cuts through the region of linear instability (cf. figure 2), while the $\alpha = 1{\cdot}25$ line is outside this region. The ticks again delineate the upper (UB) and lower (LB) solution branches.

and the one- and two-mode solutions differ markedly. These differences are illustrated in figure 5. What is most remarkable in figure 5 is the plot of E *vs.* α for the two-mode solutions. The locus of steady solutions is convoluted and at certain α's there can be as many as four solutions. One might have thought that as higher R values are approached and more modes are needed it would be the lower approximations that develop peculiarities. Instead the one-mode solution, like the first term in an asymptotic sequence, keeps its air of plausibility, while the two-mode approximation behaves strangely.

Having discussed the α variation of the energies, we now turn to their variation with Reynolds number for fixed α. Figure 6 shows E and E_U for case I as functions of R for $\alpha = 1{\cdot}00$ and $1{\cdot}25$, the former value lying within the linear stability region, the latter always outside it. In the region of $R = 10^6$ we have $E \sim R^{-\frac{1}{2}}$ and $E_U \sim R^{-\frac{2}{3}}$ as nearly as can be judged from these numerical results. Note also that for $R \gtrsim 10^6$ the disturbance flow has more energy than the mean flow. The lower branch of the E curve for $\alpha = 1{\cdot}25$ was terminated at $R = 10^4$ to simplify the diagram. The slice $\alpha = 1{\cdot}25$ was chosen for display since it both emerges near the nose of our one-mode solution surface (see figure 1) and also approximately minimizes the mean energy E_U over most of the R domain displayed.

Figures 7(*a*) and (*b*) present the case II results for energy variation with R

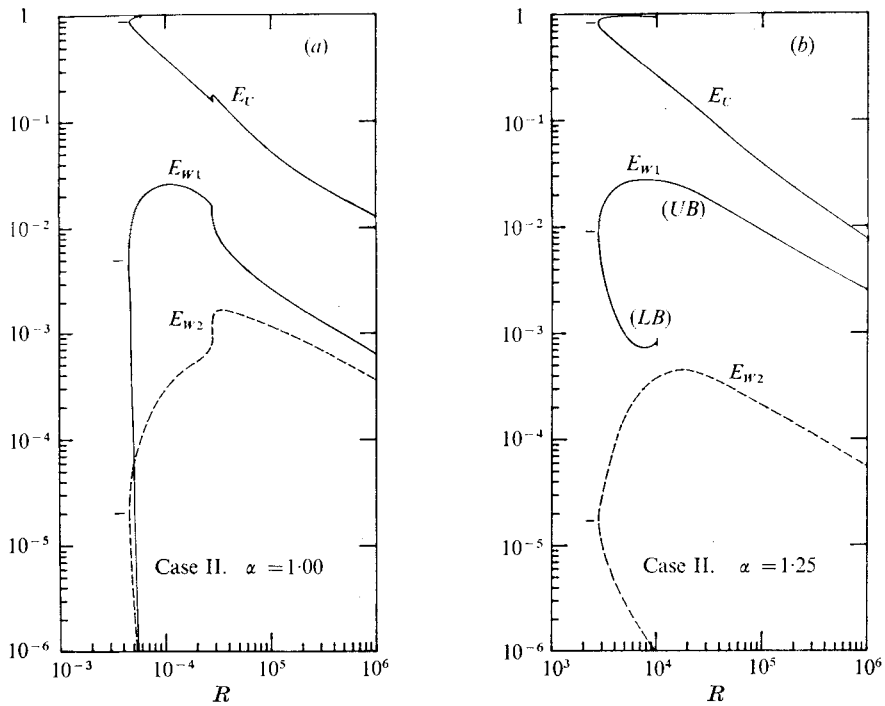

FIGURE 7. Like figure 6, this shows the energy of the steady solutions as functions of R for (*a*) $\alpha = 1{\cdot}00$ and (*b*) $\alpha = 1{\cdot}25$, but this time for case II. Here the separate contributions of the first and second modes to the total disturbance energy $E = E_{W1} + E_{W2}$ are shown

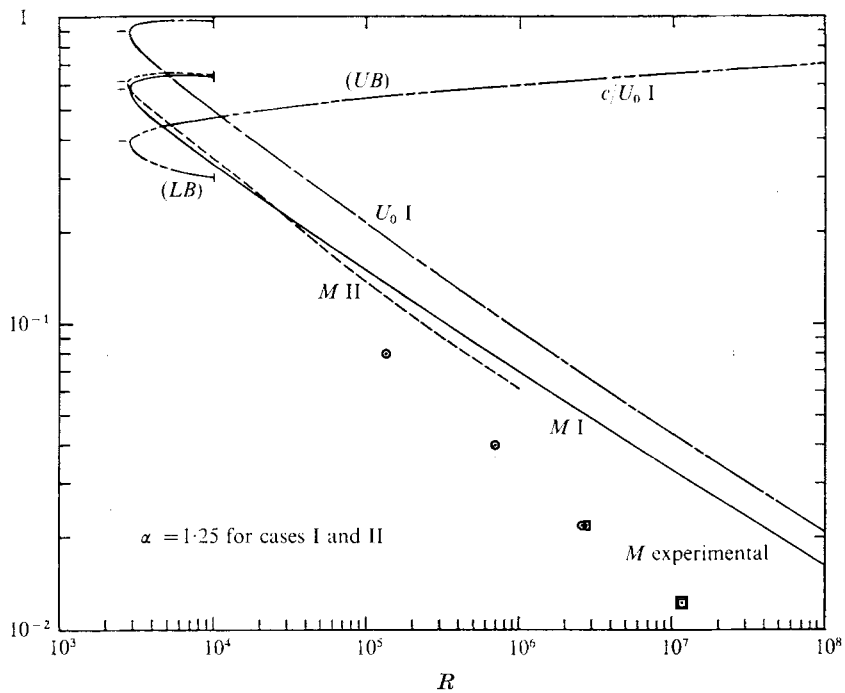

FIGURE 8. The mass flux M, maximum mean velocity U_0 and the ratio of the phase velocity c to U_0 for case I as functions of R for $\alpha = 1{\cdot}25$. Also shown for comparison is the mass flux M for case II. Experimental results for the mass flux are indicated by the circles and the squares.

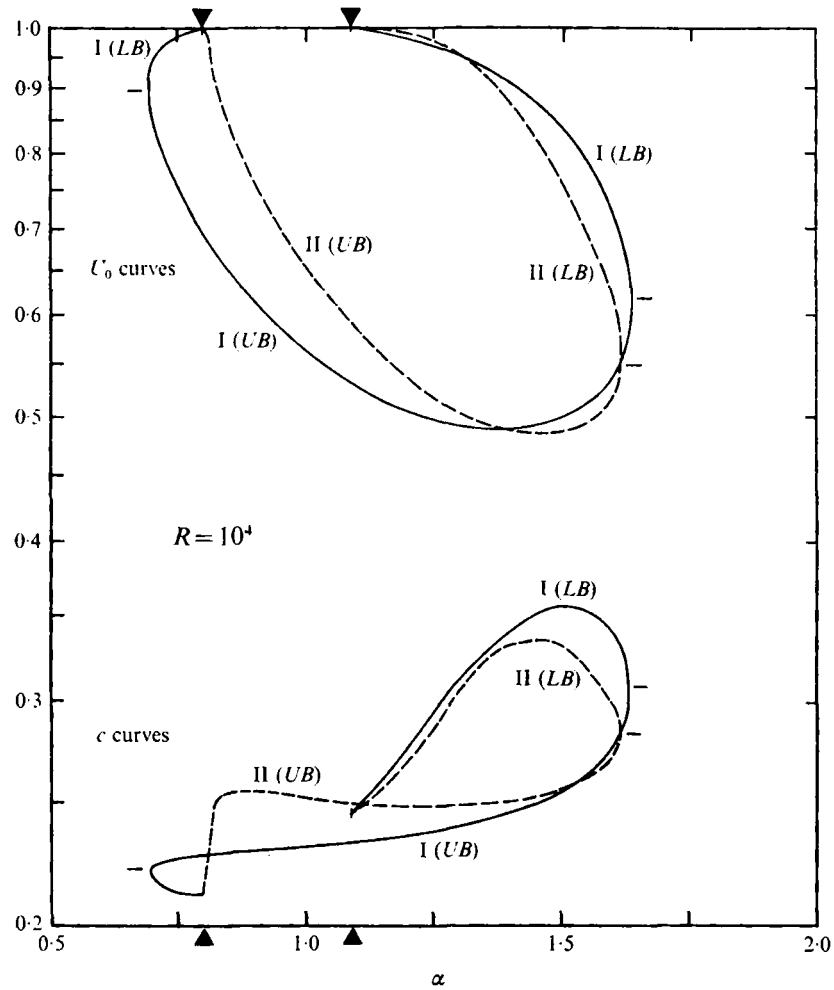

FIGURE 9. Illustrating the maximum mean velocity U_0 and phase velocity c as functions of α at $R = 10^4$ for cases I and II. The arrowheads mark the edges of the linear instability strip. The energies of these solutions are shown in figure 4.

for the wavenumbers $\alpha = 1{\cdot}00$ and $\alpha = 1{\cdot}25$ as separate panels, and distinguish the perturbation energy contributions from the first and second modes as E_{W1} and E_{W2}. As for the one-mode case, the curve for $\alpha = 1{\cdot}25$ nearly slices through the nose of the solution surface, and approximately minimizes E_U. We see that the value of R at which the two modes have comparable energies coincides with the point at which the complexities seen in figure 5 for the two-mode case begin.

Though cases I and II differ in detail as described, their gross properties remain remarkably close, as is illustrated in figure 8. The average values of the mean velocity given by the steady solutions of cases I and II are the principal features of figure 8; these are the non-dimensional mass fluxes M as defined by (2.20). For case I (one mode), the mass flux in the range $10^5 \leqslant R \leqslant 10^7$ is well fitted by $M \sim R^{-\frac{1}{8}}$, which is consistent with the previous result, $E_U \sim R^{-\frac{1}{8}}$. In the same figure the points represent experimental mass fluxes, estimated from the data

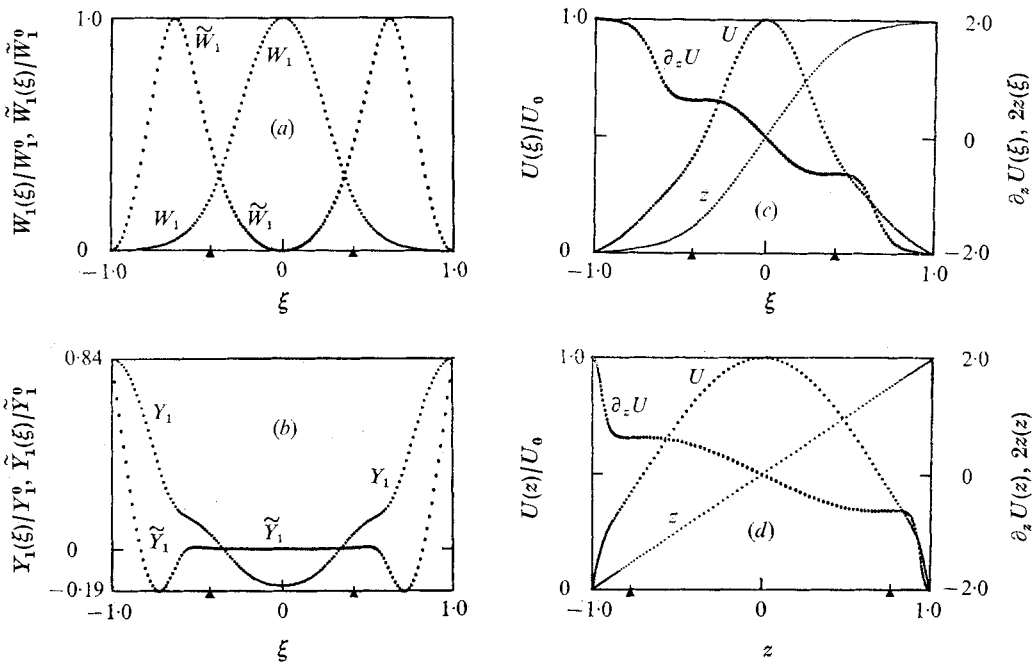

FIGURE 10. Illustrating some of the fields of the steady one-mode (case I) solution at $R = 10^4$ and $\alpha = 1{\cdot}00$. (*a*) shows the real (W_1) and imaginary ($\tilde{W}_1$) parts of the Fourier amplitude of the z component of the disturbance velocity in terms of the stretched variable ξ. (*b*) shows the corresponding parts of the y component of the disturbance vorticity. (*c*) shows the mean velocity U (in the laboratory frame) and its z derivative $\partial_z U$; also shown there is the stretching function $z(\xi)$. (*d*) repeats the mean velocity and its derivative as functions of the unstretched co-ordinate z. The arrowheads indicate the positions at which the phase velocity equals the mean velocity. The plot of $\partial_z U$ facilitates locating the inflexion points of the mean velocity profile. The normalization factors are

$$W_1^0 = 1{\cdot}07 \times 10^{-1}, \quad \tilde{W}_1^0 = 7{\cdot}38 \times 10^{-4}, \quad Y_1^0 = 11{\cdot}13, \quad \tilde{Y}_1^0 = 9{\cdot}76 \quad \text{and} \quad U_0 = 0{\cdot}562.$$

This UB solution has $E_{W1} = 3{\cdot}51 \times 10^{-2}$, $E_U = 0{\cdot}307$, $M = 0{\cdot}373$ and $c/U_0 = 0{\cdot}409$.

available and expressed in terms of the present variables; the circles represent Laufer's (1951) data while the squares are those of Comte-Bellot (1965). The points fit fairly well a law like $M \sim R^{-\frac{1}{4}}$, which does not agree with the results obtained here. Of course, in those laboratory experiments the flow was turbulent while the solutions we are attempting to approximate are laminar; hence the disparity is not surprising. (It is interesting to note that, if we require that in fully turbulent flow the dimensional mass flux be independent of viscosity, the $R^{-\frac{1}{4}}$ law results.) In figure 8 we also show as functions of R the mean velocity U_0 at mid-channel as well as the ratio of the phase velocity c to U_0 for the steady solutions of case I. The ticks on the various curves divide the UB from the LB solutions.

Figure 9 shows c and U_0 as functions of α for $R = 10^4$. The value of U_0 varies very much in the way the mean kinetic energy E_U does (see figure 4), indicating that the form of the mean velocity profile is roughly similar for the whole range of α. Perhaps more interesting is the complicated variation of c, the velocity of

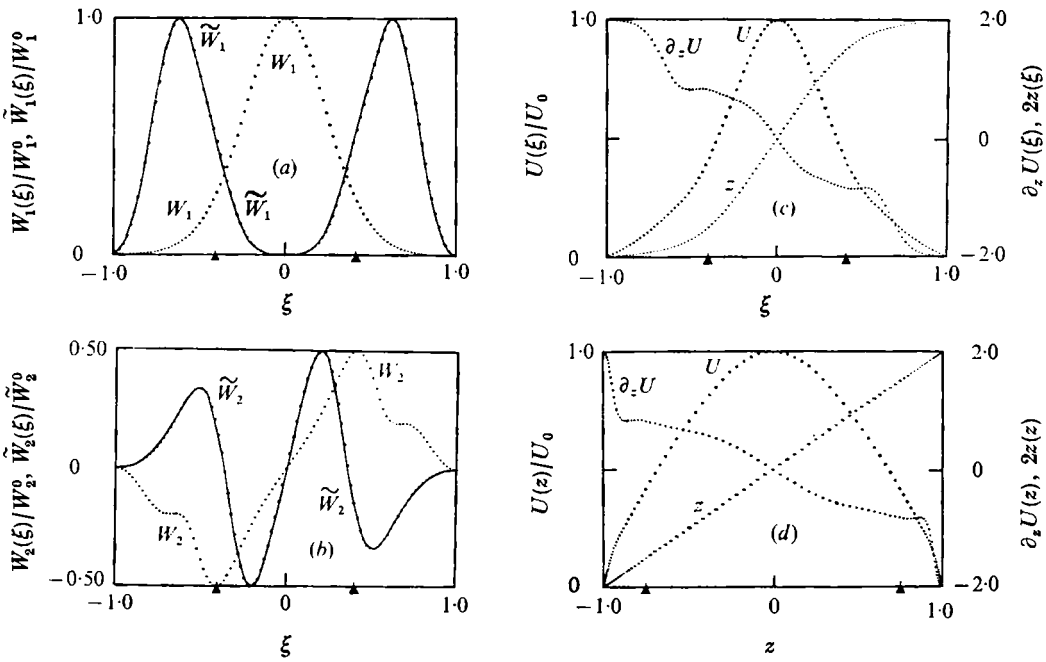

FIGURE 11. Similar to figure 10 at $R = 10^4$ and $\alpha = 1{\cdot}00$, but for the two-mode (case II) solution. However, (*a*) here shows the W's for only the first mode, while (*b*) shows those for the second mode. The vorticity is not included here as it was in figure 10. The normalization factors are $W_1^0 = 9{\cdot}36 \times 10^{-2}$, $\tilde{W}_1^0 = 7{\cdot}77 \times 10^{-4}$, $W_2^0 = 2{\cdot}34 \times 10^{-3}$, $\tilde{W}_2^0 = 1{\cdot}23 \times 10^{-2}$ and $U_0 = 0{\cdot}652$. This *UB* solution has $E_{W1} = 2{\cdot}61 \times 10^{-2}$, $E_{W2} = 3{\cdot}00 \times 10^{-4}$, $E_U = 0{\cdot}400$, $M = 0{\cdot}423$ and $c/U_0 = 0{\cdot}387$.

the reference system in which the solution appears steady, which we have also called a 'phase velocity'. The origin of this latter term, apart from its evident analogy with the phase velocity of linear theory, is explained in § 3. For the one-mode case the meaning is clear since the mode is complex and has a phase which is constant in some particular Galilean frame. For the two-mode case, the two modes have the same phase velocity for the solutions which we have characterized as steady. This common velocity c is shown in figure 9.

We note that c is systematically greater for the unstable *LB* solutions than for the *UB* solutions, but we are unable to see from this any reason for the difference in stability properties of the two solutions. We are also tempted to ask whether $dc/d\alpha$ has any physical significance, as in linear theory, but we see no real reason why it should. Nevertheless, it may be worthwhile to remark that at the transition between the *LB* and *UB* solutions $dc/d\alpha$ is positive on the *UB* side.

Let us now turn to some prototype solutions. Following a standard practice, we illustrate the results for $R = 10^4$ and $\alpha = 1{\cdot}00$. Figure 10(*a*) shows the solutions for W_1 and $\tilde{W}_1$ at these values of R and α. For this plot W_1 and $\tilde{W}_1$ have been divided by their maximum values, which are given in the caption. The forms of these fields are similar to those of the corresponding Orr–Sommerfeld eigenfunctions; however the ratio of the amplitudes of W_1 and $\tilde{W}_1$ is even less (by a

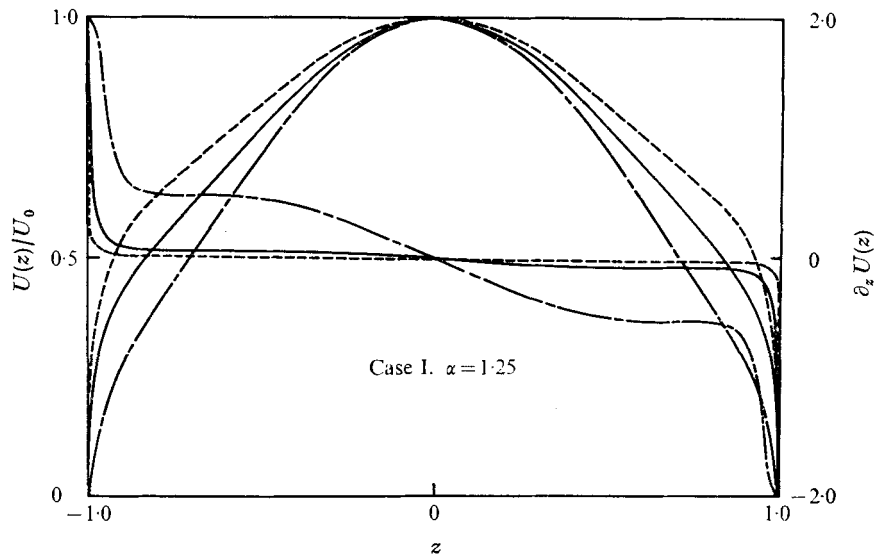

FIGURE 12. The mean velocity U profiles and their derivatives $\partial_z U$ as functions of the unstretched variable z for various R at $\alpha = 1{\cdot}25$ for the one-mode case I. The U profiles are normalized by U_0, the maximum mean velocity at mid-channel, and possess mass fluxes M.

	R	U_0	M
– — –	10^4	0·4970	0·3332
———	10^6	0·0948	0·0700
– – – –	10^8	0·0207	0·0163

factor of 3) than in the linear theory. This means that Reynolds stresses estimated from the present studies are generally less than those computed using Orr–Sommerfeld eigenfunctions as basis functions. (We chose $\tilde{W}_1(0) = 0$ for these displays so that the phases of our functions are the same as the usual linear ones.) The vorticity amplitudes Y_1 and $\tilde{Y}_1$ associated with these velocity amplitudes W_1 and $\tilde{W}_1$ [cf. (2.19)] are shown in figure 10(*b*); their magnitudes are listed in the caption and the two are comparable. In this figure, as in figures 11 and 14, the critical points at which $U = c$ are indicated by arrowheads.

We emphasize that the abscissa variable used in figures 10(*a*) and (*b*) is not z but a stretched co-ordinate ξ (cf. § 3) whose relation to z is shown in figure 10(*c*). The use of ξ as the independent variable greatly improves computational accuracy and further helps in showing the structure of the plotted solutions. Also shown in figure 10(*c*) are the mean velocity profile $U(z)$ and its z derivative $\partial_z U$. Figure 10(*d*) repeats the functions of figure 10(*c*) but shows them plotted as functions of z to give a better idea of the distorting effect of stretched variables. The U profile in this one-mode example possesses inflexion points, with sign changes in $\partial_z^2 U$, near the critical points. This feature is present in all of the case I UB solutions studied, with the exception of solutions in the immediate vicinity of the metastability nose. Thus the solutions at $R = 3 \times 10^3$ in figure 2 have no inflexion points, while the one-mode UB solutions for $R \geqslant 5 \times 10^3$, also shown

in figures 3, 4 and 5, all have inflexion points in their U profiles. Figure 10(d) also gives some idea of the distribution of the off-diagonal component of Reynolds stress. As an integral of (2.10) shows, in steady solutions the mean momentum transport is a linear function of z, and thus these off-diagonal stresses are proportional to $\partial_z U - 2z$, or to the deviation of the $\partial_z U$ curve in figure 10(d) from a line connecting the upper left to the lower right corners of the panel.

In figure 11 we show comparable fields for the two-mode case. The chief difference between this figure and figure 10 is that we do not display the vorticity functions but instead use figure 11(b) to exhibit W_2 and $\tilde{W}_2$, the velocity amplitude functions of the second mode. Compared with W_1 these are small quantities, but $\tilde{W}_2$ is much larger than $\tilde{W}_1$. This fact plays a role in determining the contributions of the two modes to the off-diagonal component of the Reynolds stress. These quantities are proportional to the Wronskians of W_1 and $\tilde{W}_1$ and of W_2 and $\tilde{W}_2$. At the value $R = 10^4$ corresponding to figure 11, the second mode contributes 5 % of the Reynolds stress as compared with 2 % at the metastability nose. The U profile for this case II solution [figure 11(c)] has inflexion points, a feature common to at least all the two-mode UB solutions at $R = 10^4$.

The effect on the mean velocity profile of increasing R is indicated in figure 12, which displays $U(z)/U_0$ and its z derivative for $R = 10^4$, 10^6 and 10^8 and $\alpha = 1{\cdot}25$ for case I. A glance below the figure at the values of U_0 shows how the flattening of the profiles increases with R even for this simple flow.

Another impression of the flow is given by the streamlines. In figure 13 we show the total stream function

$$\int_{-1}^{z} (U-c)\,dz + \Psi,$$

[cf. (2.8)] computed in the frame of steady motion for case I with $R = 10^4$ and $\alpha = 1{\cdot}00$. The most striking aspect is the meandering of the central flow (though we note also that the stretched co-ordinate is used). At the bends in the flow we find cat's-eye patterns (cf. Bergeron 1970; Stuart 1971), like the recirculating regions of both linear and small amplitude theories.

Having thus summarized cases I and II, which are approximations to two-dimensional motion, let us turn briefly to case III and three-dimensional motion. We have only explored portions of the energy surfaces for such cases and figure 14 gives a sample. It shows the intersections of the fluctuating energy surfaces of case III with the curve $\alpha R = 10^4$. The different sections are for the indicated values of the wavenumber ratio $\beta/a = \beta(\alpha^2+\beta^2)^{-\frac{1}{2}}$, and they clearly show a stabilizing effect of three-dimensionality. Such a trend was also noted by Grohne (1969). A related effect occurs in linear theory and is described by Squire's theorem; this suggests that comparison of different solutions for fixed $R\alpha$ is most revealing for the present consideration.

The solutions for a typical example of case III are shown in figure 15, which is closely analogous to figure 10. The parameters are $R = 1{\cdot}02 \times 10^4$, $\alpha = 0{\cdot}98$ and $\beta = 0{\cdot}20$. Figure 15(b) however differs from figure 10(b) in that it shows the real and imaginary parts of the z component of the vorticity amplitude function, Z_1 and $\tilde{Z}_1$. The complicated z structure of the disturbance fields may be part of

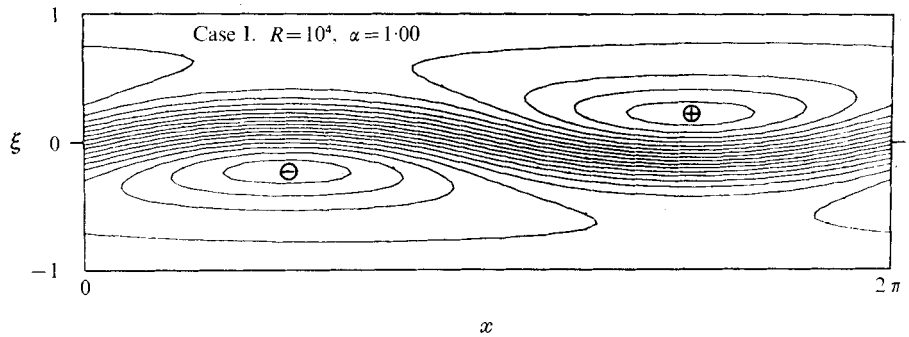

FIGURE 13. Showing streamlines for the two-dimensional case I flow detailed in figure 10. The same stretched cross-stream co-ordinate ξ is used here, but the downstream co-ordinate x is unstretched. The contours are drawn at equal intervals of the total stream function, ranging from a maximum of 0·2324 to a minimum of $-0{\cdot}2324$.

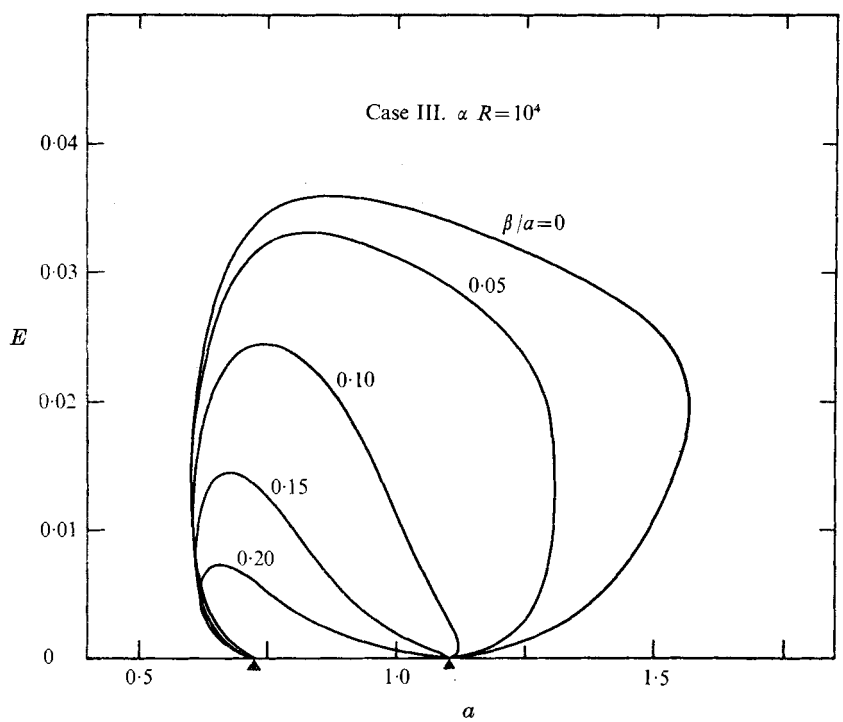

FIGURE 14. The disturbance energy E as a function of the total 'horizontal' wavenumber a for $\alpha R = 10^4$, where α is the downstream wavenumber [cf. (2.17)]. When $\beta/a = 0$, this reduces to the two-dimensional flow of case I.

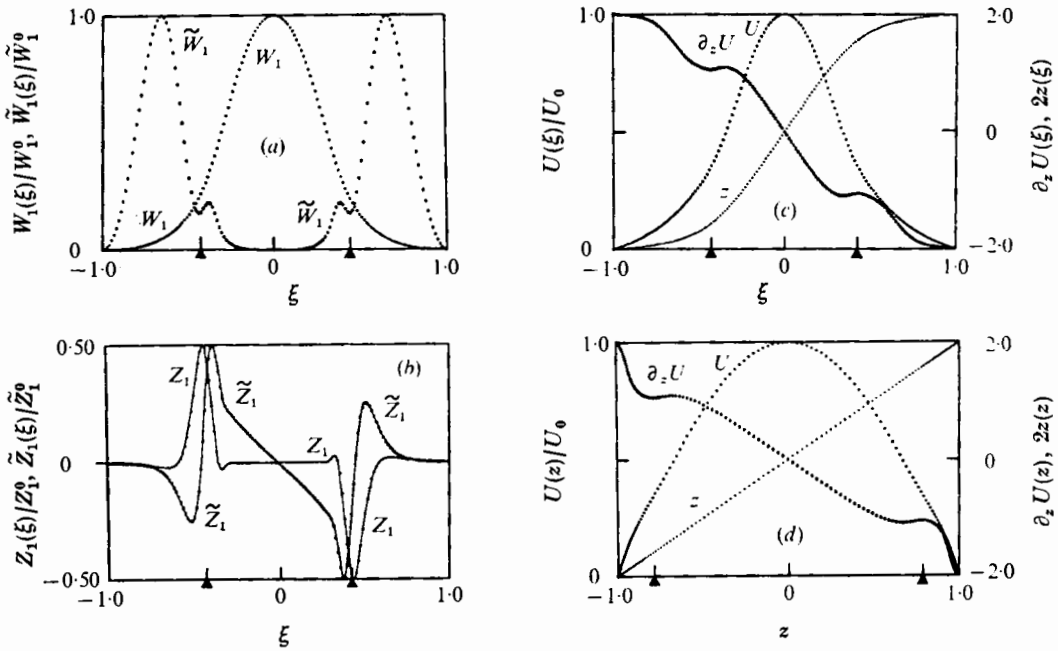

FIGURE 15. Fields for a three-dimensional solution (case III) with one mode at $\alpha R = 10^4$, $a = 1{\cdot}00$, $\beta = 0{\cdot}20$. This is like figure 10 except that here (b) gives the z component of vorticity. The normalization factors are $W_1^0 = 5{\cdot}72 \times 10^{-2}$, $\tilde{W}_1^0 = 5{\cdot}55 \times 10^{-4}$, $Z_1^0 = 0{\cdot}721$, $\tilde{Z}_1^0 = 0{\cdot}650$ and $U_0 = 0{\cdot}841$. This solution has $E_{W_1} = 1{\cdot}04 \times 10^{-2}$, $E_{z_2} = 5{\cdot}35 \times 10^{-4}$, $E_U = 0{\cdot}670$, $M = 0{\cdot}543$ and $c/U_0 = 0{\cdot}343$.

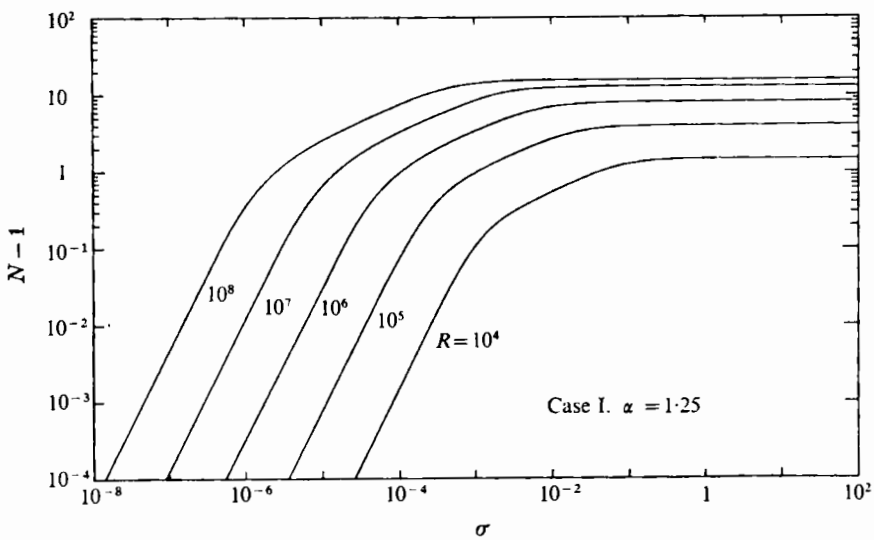

FIGURE 16. The cross-stream transport of a passive scalar quantity for the flow of case I at $\alpha = 1{\cdot}25$ and for various R. If the quantity were temperature, N would be the Nusselt number and σ the Prandtl number [cf. (2.29) and (2.30)].

the cause of the stabilization in three dimensions. We stress that the three-dimensional structures treated here are special and we cannot conclude that three-dimensionality is always stabilizing.

Finally we indicate in figure 16 how a passive scalar is transported across the channel by the one-mode velocity fields of case I. In figure 16 we plot N for various R, as a function of $\sigma = P/R$ [cf. (2.29)]. If the convected quantity is temperature, N is the Nusselt number and σ is the Prandtl number. In all cases shown, $\alpha = 1{\cdot}25$. The tendency of N to decrease with decreasing σ and the insensitivity of N to σ at large σ are both familiar in thermal convection. The slow increase of N with R at large R and σ results partly from the fact that at a fixed α we move out of the main part of the metastable region as R increases. Moreover, the Nusselt number should vary approximately like the square root of the disturbance energy E, which in turn varies like $R^{-\frac{1}{5}}$ at the values considered here. In particular, these curves are well represented by $N-1 \sim \sigma^2 R^{\frac{3}{5}}$ for $\sigma^2 R^{\frac{3}{5}} < 0{\cdot}1$.

5. Conclusions

The equations solved in this work are only an approximation to the Navier–Stokes equations. We nevertheless believe that the solutions obtained correspond qualitatively to solutions of the Navier–Stokes equations. For $R \lesssim 10^4$ the structure of solutions in parameter space is entirely in accord with what one would expect to find on the basis of small amplitude theory. Moreover, in the metastable regime the small amplitude (or LB) solutions are unstable in agreement with the findings of Chen & Joseph (1973). Though we cannot make a conclusive statement about the stability of the large amplitude (UB) solutions, we certainly could not permanently dislodge them with the perturbations we could make to them. If the UB solutions of these calculations are indeed stable at the lower Reynolds numbers, their failure to appear in experiments is surprising, and apparently at variance with Landau's (1944) view of the transition to turbulence.

Landau suggested that, following an instability of the laminar state, a disturbance flow develops to the point where the nonlinear terms limit its amplitude as described by (1.1). As the degree of instability is increased, this solution in turn becomes unstable, and turbulence grows out of a sequence of such instabilities. Since the solutions of (1.1) have been found to be unstable, the suggestion is not correct in detail. The UB solutions might have provided the missing ingredient for Landau's picture, but this is not what experiments show in channel flow. There does not seem to be anything that could be taken to be analogues of Bénard cells, to take a case where Landau's ideas seem to have more relevance. It would be of interest to know why these different kinds of transition to turbulence exist.

It may well be that the potential analogues to cellular motion, the UB solutions, are always unstable. Alternatively, such solutions may be precursors to bursts as in Landahl's (1972) view. Possibly, different precursor solutions exist and suppress the UB solutions found here. A contender for this role is the kind

of solution discussed by Stewartson & Stuart (1971) which, in effect, allows for spatial modulation of the downstream wavenumber. In any case, the work reported here seems to make the contrast between the transitions to channel flow turbulence and to (say) thermal turbulence more graphic.

We thank Dr Eric Graham for numerous useful discussions, and in particular for asking the several crucial questions that led us to implement the boundary conditions in the current manner. Dr Robert Jastrow kindly extended to us the hospitality and the extensive computing facilities of the Goddard Institute for Space Studies. The helpful comments of Dr J. Trevor Stuart to this paper are acknowledged. This work was also supported in part by the National Science Foundation under grants NSF GP 32336x and GP 27209. A considerable portion of this work was completed after J.-P.Z. returned to the Observatoire de Nice and J.T. joined the Department of Astro-Geophysics and the Joint Institute for Laboratory Astrophysics, University of Colorado.

REFERENCES

BERGERON, R. F. 1970 Some inviscid 'cat's eye' flows. *Studies Appl. Math.* **49**, 197–203.

BUSSE, F. H. 1967 On the stability of two-dimensional convection in a layer heated from below. *J. Math. & Phys.* **46**, 140–150.

CHEN, T. S. & JOSEPH, D. D. 1973 Subcritical bifurcation of plane Poiseuille flow. *J. Fluid Mech.* **58**, 337–351.

COMTE-BELLOT, G. 1965 Écoulement turbulent entre deux parois parallèles. Ph.D. thesis, University of Grenoble.

DOWELL, E. H. 1969 Non-linear theory of unstable plane Poiseuille flow. *J. Fluid Mech.* **38**, 401–414.

ECKHAUS, W. 1965 *Studies in Non-linear Stability Theory*. Springer.

GEORGE, W. D. & HELLUMS, J. D. 1972 Hydrodynamic stability of plane Poiseuille flow with finite amplitude disturbances. *J. Fluid Mech.* **51**, 687–704.

GROHNE, D. 1969 Die Stabilität der ebenen Kanalströmung gegenüber dreidimensionalen Störungen von endlicher Amplitude. *AVA Göttingen Rep.* 69-A-30.

HENRICI, P. 1962 *Discrete Variable Methods in Ordinary Differential Equations*. Wiley.

LANDAHL, M. T. 1972 Wave mechanics of breakdown. *J. Fluid Mech.* **56**, 775–802.

LANDAU, L. 1944 On the problem of turbulence. *C. R. Acad. Sci. U.R.S.S.* **44**, 311–314.

LAUFER, J. 1951 Investigation of turbulence in a two-dimensional channel. *N.A.C.A. Tech. Rep.* no. 1053.

LIN, C. C. 1955 *The Theory of Hydrodynamic Stability*. Cambridge University Press.

MEKSYN, D. & STUART, J. T. 1951 Stability of viscous motion between parallel planes for finite disturbances. *Proc. Roy. Soc.* A **208**, 517–526.

MONIN, A. S. & YAGLOM, A. M. 1971 *Statistical Fluid Mechanics* (ed. J. L. Lumley). M.I.T. Press.

ORSZAG, S. A. 1971 Accurate solution of the Orr–Sommerfeld stability equation. *J. Fluid Mech.* **50**, 689–703.

PEKERIS, C. L. & SHKOLLER, B. 1967 Stability of plane Poiseuille flow to periodic disturbances of finite amplitude in the vicinity of the neutral curve. *J. Fluid Mech.* **29**, 31–38.

PEKERIS, C. L. & SHKOLLER, B. 1969*a* Stability of plane Poiseuille flow to periodic disturbances of finite amplitude. *J. Fluid Mech.* **39**, 611–627.

PEKERIS, C. L. & SHKOLLER, B. 1969*b* The neutral curves for periodic disturbances of finite amplitude of Poiseuille flow. *J. Fluid Mech.* **39**, 629–639.

PEKERIS, C. L. & SHKOLLER, B. 1971 Stability of plane Poiseuille flow to periodic disturbances of finite amplitude. II. *Proc. Nat. Acad. Sci.* **68**, 197–199.

REYNOLDS, W. C. & POTTER, M. C. 1967 Finite-amplitude instability of parallel shear flow. *J. Fluid Mech.* **27**, 465–492.

STEWARTSON, K. & STUART, J. T. 1971 A non-linear instability theory for a wave system in plane Poiseuille flow. *J. Fluid Mech.* **48**, 529–545.

STUART, J. T. 1960 On the non-linear mechanics of wave disturbances in stable and unstable parallel flows. Part 1. The basic behaviour in plane Poiseuille flow. *J. Fluid Mech.* **9**, 353–370.

STUART, J. T. 1971 Nonlinear stability theory. *Ann. Rev. Fluid Mech.* **3**, 347–370.

THOMAS, L. H. 1953 The stability of plane Poiseuille flow. *Phys. Rev.* **91**, 780–783.

VERONIS, G. 1966 Motions at subcritical values of the Rayleigh number in a rotating fluid. *J. Fluid Mech.* **24**, 545–554.

VERONIS, G. 1968 Effect of a stabilizing gradient of solute on thermal convection. *J. Fluid Mech.* **34**, 315–336.

WATSON, J. 1960 On the non-linear mechanics of wave disturbances in stable and unstable parallel flows. Part 2. The development of a solution for plane Poiseuille flow and plane Couette flow. *J. Fluid Mech.* **9**, 371–389.